Check for updates

Arrhenius plots for Li-ion battery ageing as a function of temperature, C-rate, and ageing state – An experimental study

Gints Kucinskis [a,b,1], Maral Bozorgchenani [a,1], Max Feinauer [a], Michael Kasper [a], Margret Wohlfahrt-Mehrens [a], Thomas Waldmann [a,*]

[a] ZSW – Zentrum für Sonnenenergie- und Wasserstoff-Forschung, Baden-Württemberg, Helmholtzstrasse 8, D-89081 Ulm, Germany
[b] Institute of Solid State Physics, University of Latvia, Kengaraga Street 8, Riga, LV, 1063, Latvia

HIGHLIGHTS

- Commercial 21,700 cells and lab-made pouch cells with similar N/P ratios compared.
- Cycle life estimation by Arrhenius plots as a function of temperature, C-rate & SoH.
- Temperature for optimum cycle life shifts with C-rate & SoH.
- Anode loading and particle size affects optimum cycling conditions.
- Non-linear capacity fade leads to changes of Arrhenius plots during aging.

GRAPHICAL ABSTRACT
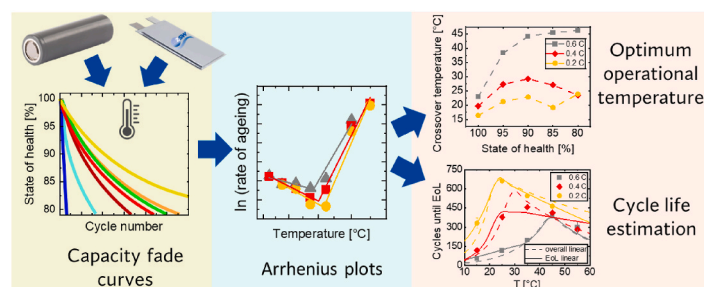
ABSTRACT

We present an extensive analysis of Li-ion battery ageing via Arrhenius plots. The V-shaped Arrhenius plots show minima at an optimum temperature corresponding to the longest cycle-life. The V-shape of the Arrhenius plots signifies the crossover between the two dominating ageing mechanisms – solid electrolyte interphase (SEI) growth in the high temperature range and lithium deposition in the low temperature range. Subjects of our investigations are commercial 5 Ah high energy 21,700-type cells with $LiNi_{0.90}Co_{0.05}Al_{0.05}O_2 + LiNiO_2$ (NCA + LNO) cathode and Si/graphite anode (~3% Si) and 0.1 Ah lab-made pouch cells with $LiNi_{1/3}Mn_{1/3}Co_{1/3}O_2$ (NMC111) cathode and a graphite anode. The results of the Arrhenius plots are analysed in the context of C-rate, cell ageing, and electrode properties. We find that the crossover between the dominating ageing mechanism and hence the optimum operating temperature of the Li-ion cells depend on C-rate, anode coating thickness/particles sizes, the state of health, and the shape of the capacity fade curve. Considering the change of the dominant ageing mechanism can help designing battery systems with longer service life. Additionally, we show a lifetime estimation for temperature dependent cycling of batteries emphasizing the merit of Arrhenius plots in the context of battery cell ageing.

* Corresponding author.
  E-mail address: thomas.waldmann@zsw-bw.de (T. Waldmann).
[1] These authors contributed equally.

1. Introduction

Li-ion batteries (LIBs), currently the most popular energy storage technology, are powering electric vehicles, portable electronic devices and power tools, and are also used to provide grid-level energy storage. While service life of a battery cell is a key parameter for all rechargeable batteries, ageing characteristics become even more crucial with the exponentially rising number of LIBs produced and the consequent sustainability concerns [1].

Over time, as LIBs age, their capacities fade and the internal resistances increase. It is typically expected for LIBs to remain functional over the span of several years, with the discharge capacity remaining above 80% of the initial value – this is referred to as 80% state of health (SoH). While the battery can remain operational long after 80% SoH is reached, this is often considered a crucial milestone in its lifetime.

The main ageing mechanisms of battery cells are a growth of a solid-electrolyte interface (SEI) and lithium deposition on the anode (and with it – loss of lithium inventory (LLI) [2–5], depleting the amount of lithium able to participate in the charge-discharge reactions) [6–9]. Other mechanisms include loss of active anode or cathode material either due to loss of contact between particles or changes in the crystal structure of the active material [10–12].

Efforts have been made to parametrize and model the ageing of battery cells [13–15]. Different groups have suggested that the main ageing mechanism can intensify or change during ageing [15–20]. The change of the ageing mechanism influences the shape of the capacity fade curve, i.e. instead of being linear, it becomes either accelerated or deaccelerated [7]. Possible reasons leading to an accelerated capacity fade can be drying of the electrolyte in the cell [21], pore clogging [16], or Li deposition [19] in the later stages of ageing. A reason for decelerated capacity fade can be LLI due to side reactions [2–5] and therefore a lower susceptibility to Li deposition in later stages of ageing [18,20].

Arrhenius plots are well known from textbooks [22,23] for the description of the temperature dependency of chemical reactions. The same principle has been applied to battery ageing by different groups for the capacity decrease [24], power decrease [25], and impedance increase [24,26,27] for temperatures ≥ 25 °C. Arrhenius equation (1) describes a rate constant as a function of temperature [22,23]. In this case, we use the Arrhenius equation to describe the rate of ageing

$$r = A \cdot \exp\left(-\frac{E_a}{k_B T}\right) \qquad (1)$$

with A being a pre-exponential factor, E_a the activation energy, k_B the Boltzmann constant, and T the absolute temperature.

We have previously shown that two distinct branches in the Arrhenius plot can be observed when the investigation is extended across a wider temperature range, especially when including low temperatures, e.g. 0 °C. These two branches correspond to SEI growth in the high temperature region (i.e. typically above ~25 °C for medium C-rates) and Li deposition in the low temperature region (i.e. typically below ~25 °C for medium C-rates) [6]. While the ageing behaviour can vary depending on the cell chemistry, the general trend with two distinct ageing mechanisms remains [28,29].

Our group previously used 3-electrode pouch full cells reconstructed from commercial 16 Ah pouch cells to demonstrate that the main criterion enabling Li deposition thermodynamically is an anode potential lower than 0 V vs. Li/Li$^+$ [30]. The study showed experimentally that Li deposition is more prevalent at low temperatures and high C-rates [30]. A theoretical study by Yang and Wang concluded that the dominating ageing mechanism indeed depends on both temperature and charging rate [31]. Similar calculations have recently been carried out by Liang et al. [32]. We were able to confirm this phenomenon experimentally, demonstrating two distinct Arrhenius-type ageing behaviours for both high-energy commercial 21,700 cylindrical cells and lab-built pouch cells, with the crossover temperature between both branches in the Arrhenius-plot shifting depending on the charging rate and anode thickness [33].

In this work, we build on our previous study and analyse ageing of commercial 21,700 cells and lab-built pouch cells to evaluate in depth, how the dominating ageing mechanism shifts with C-rate, temperature, cell parameters, and SoH. Furthermore, an estimation of the end of life (EoL) criterion at a SoH of 80% is performed based on the Arrhenius plots. By analysing the ageing behaviour as a function of a large set of parameters, this work enables deriving optimized charging protocols to ensure optimum service life of battery cells.

2. Experimental

2.1. Commercial cylindrical cells

Two types of cells were used in the experiments – commercial cylindrical and lab-made pouch cells. The electrode parameters for both types of cells are given in Table 1. For the commercial 21,700 cells, a Post-Mortem analysis on a fresh cell after discharging the cell to 2.5 V was performed. Samples were washed with DMC. The electrodes were analysed by scanning electron microscopy (SEM), energy dispersive X-ray (EDX) analysis, inductively coupled plasma optical emission spectroscopy (ICP-OES, Arcos SOP, Spectro), and Hg intrusion porosimetry (PASCAL 140–440 Series, Porotec).

EDX suggests that the anode consists of graphite with ~3% Si. SEM, ICP-OES, and EDX suggest that the cathode of the commercial cells is NCA (LiNi$_{0.90}$Co$_{0.05}$Al$_{0.05}$O$_2$) with ~6% LiNiO$_2$ (LNO). LNO might originate from Li$_2$NiO$_2$ which was most likely used as a sacrificing cathode material to increase the amount of Li for pre-lithiation of the Si compound in the anode [33–36].

Masses per unit area in g cm^{-2} of anode and cathode were determined from punched-out test samples (10 cm^2) in combination with weighing. Areal loadings in mAh cm^{-2} and N/P ratios were estimated from the determined areal masses, and reasonable values from literature for NCA (200 mAh g^{-1}) [37,38], LNO (80 mAh g^{-1}) [36], graphite (320 mAh g^{-1}) [39–41], Si (1000 mAh g^{-1}) [42].

We would like to note that we had estimated the single-sided anode coating thickness for the 21,700 type of commercial cells via ref. [43] from the specific energy of 262 Wh kg^{-1} to be 93 ± 4 μm [44], which agrees well with the value of 86 μm measured after Post-Mortem analysis in the present paper when the presence of a Si compound is considered.

50 commercial cylindrical 21,700 cells with the same lot number

Table 1
Cell design information and key parameters of the electrodes. The given values for the areal loadings and the N/P ratio for the commercial cell are rough estimations.

Parameter	Commercial cell (cylindrical)		Lab-made cell (pouch cell)	
	Anode (Graphite + Si)	Cathode (NCA + LNO)	Anode (Graphite)	Cathode (NCM111)
Particle size [μm]	graphite: ~2 to 25 Si: ~10	~2 to 20	~1 to 12	~5 to 10
Single sided coating thickness [μm]	86	66	58	52
Initial porosity [%]	30	25	30	33
Areal loading [mAh cm^{-2}]	~5.4	~4.3	2.50	2.06
Negative-Positive (N/P) ratio	~1.2		1.21	
Nominal capacity [Ah]	5.0		0.1	

were investigated. Internal resistance (Hioki RM3548 at 1 kHz, (12.9 ± 0.3) mΩ), mass ((69.5 ± 0.1) g), and voltage ((3.679 ± 0.002) V) were determined. The low standard deviations show that the cells are very similar and can be used for further tests. Vötsch and CTS climate chambers and BaSyTec CTS testers were used to perform long-term cycling at ambient temperatures in the range of −15 °C to +55 °C. Charge rates of 0.2C, 0.4C, and 0.6C were used in constant current - constant voltage (CC-CV) mode until 0.05C. Discharge rates of 0.5C (CC) were used. The 21,700 cells were cycled in the range of 2.5 V–4.2 V. At least two cells were cycled per condition to assure repeatability, with the exception being 55 °C where only one cell was cycled for each C-rate and temperature. During cycling, cells were allowed to rest for 5 min after charging and 30 min after discharging.

2.2. Lab-made pouch cells

Bilayer pouch cells were built with a capacity of ~0.1 Ah. The values shown in Table 1 for the lab-made pouch cells were obtained by characterizing pristine electrodes before building the cells. Anode, cathode, and separator were double side coated graphite (2.50 mAh cm^{-2}), single side coated LiNi$_{1/3}$Mn$_{1/3}$Co$_{1/3}$O$_2$ (NMC111, 2.06 mAh cm^{-2}), and Celgard 2325, respectively. The electrodes were vacuum dried at 130 °C for 9 h. The pouch cells were assembled in a dry room (dew point < −62 °C). After the assembly of the pouch cells, the cells were dried in an antechamber of an Ar-filled glove box (MBraun, O$_2$ and H$_2$O < 0.3 ppm) at 80 °C for 16 h. The electrolyte filling was performed in an Ar-filled glove box with 900 μL 1.0 M LiPF$_6$ in EC:EMC (3:7 wt) + 2% VC. All electrochemical tests were carried out by BaSyTec CTS and Maccor 4200 systems in climate chambers (Vötsch, CTS). Formation was performed after 12 h rest time for wetting purposes. We performed three cycles with 0.1C in the full voltage range of 2.7 V–4.2 V at 25 °C. For charging a CC-CV protocol with CV until 0.05C and for discharging a CC protocol was used. Rest times of 30 min were allowed after each charging and discharging of the cell.

Ageing of the lab-made pouch cells was performed at ambient temperatures in the range of −15 °C to +60 °C. Cycling ageing was performed at charging rates of 0.2C, 0.5C, and 1C (CC-CV, CV until 0.02C). Charge and discharge steps used the same C-rates. During the electrochemical measurements, the cells were mechanically pressed using a cell holder to apply a uniformly distributed force of ~100 N perpendicular to the electrode layers.

3. Results and discussion

3.1. Cell parameters

The parameters of both cell types are shown in Table 1. The thickness of the electrodes is larger in the commercial cell compared to the lab-made pouch cells while the porosities of the anodes used in both cells are very similar (30%). The areal loading is consequentially about twice as large for the commercial cell. Given that an electrode with a thicker coating leads to increased areal current density, thicker anodes of comparable composition and porosity are expected to show a higher tendency to lithium deposition.

According to SEM measurements (Fig. S3), the particle sizes for the electrodes of the fresh commercial cell are ~2–20 μm for the cathode and ~2–25 μm for the partly flaky and potato-shaped graphite particles of the anode. The particle size of the Si component in the anode of the commercial cell is in the order of ~10 μm (Fig. S4). The particle sizes in the cathode and anode (non-spherical graphite) of the lab-made pouch cells were ~5–10 μm and ~1–12 μm, respectively.

Another important parameter is the negative-positive (N/P) ratio, which is very similar for both types of cells used in this study (see Table 1). Lower N/P ratios make cells more prone to lithium deposition [45], as the lithium concentration in the surface of the anode can more easily reach the point of complete saturation – a widely recognized

condition for lithium deposition [30,46]. The N/P ratios of both cells, however, are relatively high and most likely very similar in the present study. We stress that in case of the commercial cells, assumptions have been made which are described in the experimental part. Therefore, the areal loadings and the N/P ratio of the commercial cells should be regarded as a rough estimation. To facilitate further discussion and eventual later simulation studies, all cell parameters are listed in the Table 1 which is similar to the table in the simulation study on Arrhenius plots by Yang and Wang for other cell types [31].

3.2. Capacity fade behaviour

Both, commercial and lab-made pouch cells, were cycled at various temperatures and C-rates. The obtained capacity fade curves (Fig. 1) show normalized discharge capacity curves (SoH) as a function of cycle number. This is the dataset used for further analysis of the results. The same data are shown in Supplementary Fig. S1 and Fig. S2. There, to aid later discussion, selected data are sorted by temperature and plotted versus cycle number and ageing time, respectively.

While Fig. 1 is dominated by decelerated capacity fade curves (especially in the high temperature region), accelerated capacity fade is mostly observed at lower temperatures – compare e.g. curves obtained at 1C in Fig. 1f to see a gradual shift from the accelerated to decelerated shape as the temperature is increased from −10 °C to 60 °C. When the temperature is kept constant, the curve shifts from decelerated to accelerated shape with increasing C-rate (best seen in Fig. S1f).

As discussed in Ref. [7], the shape of the capacity fade curve is most likely governed by the dominating ageing mechanism. In general, the shape of the curves can be grouped into accelerated, decelerated or linear, as shown schematically in Fig. 2. Typical examples for all curve shapes can be seen in Fig. 1a: at 15 °C (green) and below a fast accelerated ageing behaviour, at 25 °C a slow linear ageing behaviour (yellow) and at 35 °C (orange) and above a slow decelerated aging behaviour.

Petzl et al. showed that when decelerated ageing behaviour is observed, the capacity loss is most likely related to LLI, as the fully intercalated state of the electrodes cannot be reached anymore [20]. Lithium is mostly trapped in the SEI, which is driving the ageing of battery cells at higher temperatures [6,44]. On the other hand, an accelerated trend is observed mostly in the case of lithium deposition, which takes place during the charging of the cell. Both ageing mechanisms are discussed in more detail further on in the text.

Interestingly, capacity fade curves of commercial cells converge at higher temperatures despite the different charging rates (Fig. S1d and Fig. S1e) – in other words, the rate of ageing displays diminishing C-rate dependence. High temperature capacity fade curves of lab-made cells show high time-dependence (see Fig. S2, most notably in Figs. S2h–j) and hint to the calendar ageing being a more significant factor than the cycle number for the lab-made cells in this study.

3.3. Arrhenius plots

To evaluate the ageing behaviour in more detail, we plotted Arrhenius-type graphs according to eq. (1), where a natural logarithm of the ageing rate r is plotted as a function of inverse temperature ($1/k_BT$). The ageing rate r is measured in percent per cycle and is determined by the slope of capacity fade curves (Fig. 1), calculated at a particular SoH. The method for calculating the ageing rate is shown in Fig. 2. Typically, 20 cycles before and after the pre-defined SoH value are used and ensure a good quality of the linear fit even if the total ageing behaviour is strongly non-linear. To calculate the ageing rate at 100% SoH, the first 40 cycles were used for fitting. We note that the Arrhenius plots in this study were evaluated from capacity fade vs. cycle diagrams rather than vs. time because different C-rates were investigated. The constructed Arrhenius plots are shown in Fig. 3.

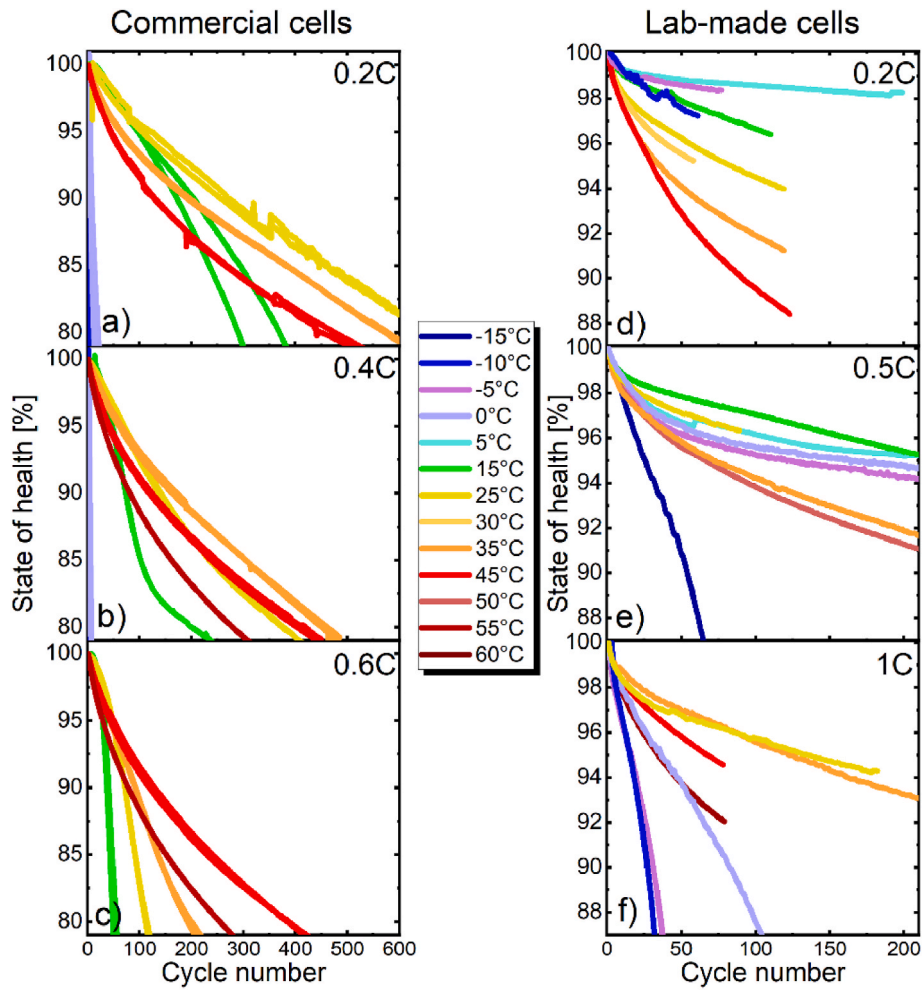In case of rapid ageing, the number of cycles used for the fit is

Fig. 1. Capacity fade curves of commercial cells charged at (a) 0.2C, (b) 0.4C and (c) 0.6C rate and lab-made cells charged at (d) 0.2C, (e) 0.5C and (f) 1C rate.
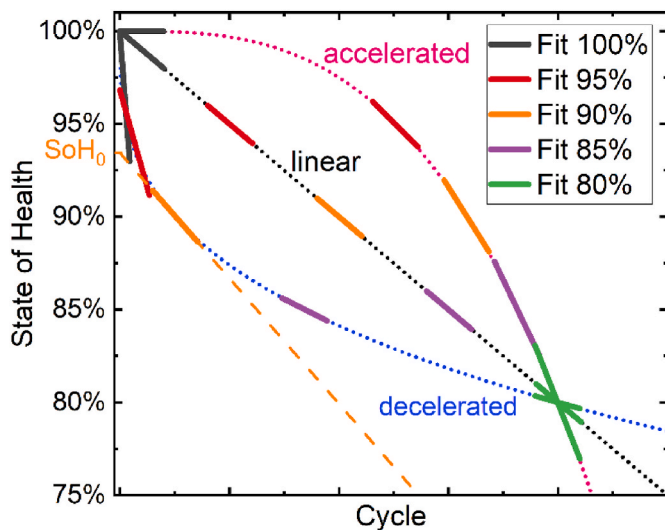

Fig. 2. Schematic explanation of the linear fits of the dotted ageing curves at different SoH for three typical ageing behaviours (linear, accelerated and decelerated). The fitted straight line for 90% SoH of the decelerated ageing curve is drawn (dashed orange line) to illustrate the slope defining the ageing rate *r* and the y-intercept defining SoH$_0$. (For interpretation of the references to colour in this figure legend, the reader is referred to the Web version of this article.)

reduced to clearly distinguish between different SoH regions. If the SoH changed by more than 5% over the 20 or 40 cycles used for fitting, the linear fit was performed only by using the cycles within the 5% SoH range. At least two cycles before and after the desired SoH were always used for fitting, i.e. at least three cycles for 100% SoH and five cycles for all other considered SoH values. If a very rapid ageing is experienced by the cell (most measurements obtained at 0 °C and below, see Fig. 1), the adjacent fits at 100% SoH, 95% SoH, 90% SoH, and beyond can often include common data points, as schematically shown in Fig. 2 for the decelerated capacity fade curve. Hence, due to the rapid ageing, r values calculated for ambient temperatures of 0 °C and below should be viewed mostly as a qualitative indication of the general trend.

In the Arrhenius plots in Fig. 3 the two branches for low and high temperature are clearly visible for all measured cells across all SoHs, cell types, and C-rates. The two lines used to fit the data points form distinct V shapes. We would like to note that the change between the two main aging mechanisms is most likely not as sharp as suggested by the V-shape of the Arrhenius plot. It is instead a smoother transition with both mechanisms active to a lower extent at the minimum. One limitation of Arrhenius plots is that they indicate the main mechanisms of ageing, and not minor mechanisms (e.g. delamination) which most likely take place in parallel.

The observations of two Arrhenius-type relations are in good agreement with our group's previous results [6,28,44]. At the inter-section of both lines fitting the trends in the Arrhenius plots is the minimum ageing rate and hence the longest expected cycle life. We call the temperature where this minimum is reached the crossover
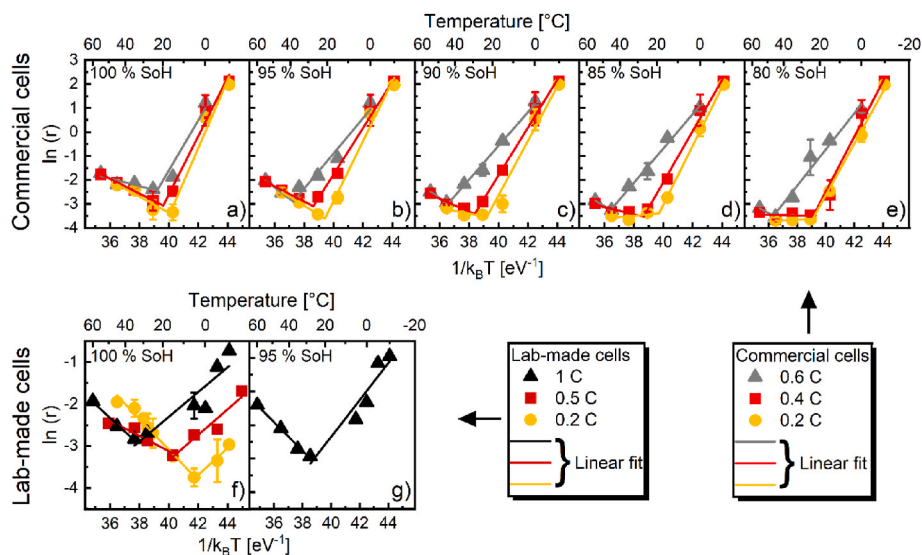
Fig. 3. Arrhenius plots showing the ageing behaviour of commercial cells at (a) 100% SoH, (b) 95% SoH, (c) 90% SoH, (d) 85% SoH and (e) 80% SoH as well as the ageing behaviour of lab-made cells at (f) 100% SoH and (g) 95% SoH for different C-rates. Linear fits of the low and high temperature region are plotted as solid lines.

temperature, as the dominating ageing mechanism is changing at this temperature.

For the commercial 21,700 cells at 0.2C, the minima in the Arrhenius plots are shifted to higher temperatures compared to the lab-made pouch cells. This is consistent with simulations by Yang and Wang [31] and with a larger amount of lithium deposition found on anodes with higher loading by Gallagher et al. [47]. These results indicate that high-energy cells most likely show a stronger susceptibility to lithium deposition compared to high-power cells.

In absolute numbers, the optimum or crossover temperature at a similar C-rate is much smaller for lab-made pouch cells. For example, while at 0.2C charge rate and 100% SoH pouch cells age slowest at 6 °C, the crossover and hence optimum temperature for commercial cylindrical cells is 16 °C. This is related to the relatively lower areal loading of the anode in lab-made cells (2.50 mAh·cm^{-2}) compared to the areal loading of the anode in commercial cells (5.38 mAh·cm^{-2}). The higher areal loading of the commercial cells in combination with the tendency to larger anode particles make these more susceptible to lithium deposition. We note that the N/P ratio, another important factor that could influence the susceptibility to lithium deposition, is likely similar for both types of cells (Table 1).

For virtually all SoHs and both cell types, the crossover between the dominant ageing mechanisms shifts to higher temperatures as the C-rate is increased. This is similar to the ageing behaviour previously simulated by Yang and Wang [31]. It is also a logical conclusion when considering that lithium deposition occurs due to the limitations of Li diffusion within the graphite anode [33]. In general, lithium deposition occurs because of insufficiently fast Li diffusion within the anode, leading to a complete lithiation of the surfaces of graphite particles and also of the anode surface while leaving the deeper layers and inner parts of the particles with lower amounts of lithium [48,49]. If charging of the battery is continued, instead of being inserted in the electrode, a part of the lithium is deposited on the surface of the anode [50–53].

For the commercial cells, when the high and low temperature Arrhenius branches are compared, the slope is steepest for the low temperature line, especially at 0.4C and 0.2C. Practically speaking, an increase in C-rate has a significant influence on the ageing rate of the cells at low temperatures, whereas the ageing rates in the higher temperature region display a weaker C-rate dependence. This is consistent with the overlap of the capacity fade curves at high temperatures shown Figs. S1d and e and indicate that lithium deposition is more rate-dependent than the cell ageing at higher temperatures, which is

caused predominantly by SEI growth on the anode [6]. Note, however, that SEI growth depends on many factors beyond the C-rate, such as temperature, time, and SoH [8,54–56], which will be discussed further in the text.

For the lab-made cells, the slope of the low temperature Arrhenius line is less steep (Fig. 3f and g) compared to the commercial cells (Fig. 3a–e). This could be affected by the lower single-sided anode coating thickness of the lab-made cells of 58 μm in comparison with 86 μm of the commercial cells and the particles sizes which are smaller for the lab-made pouch cells (Table 1). However, effects of the material cannot be excluded here [6]. Although the general trend of crossover temperature increasing as a function of C-rate remains, opposite to the commercial cells, the impact of increasing C-rate is comparable for low and high temperatures.

We further analysed the ageing rate as a function of SoH. Consistent with the decelerating shape of most of the capacity fade curves, the Arrhenius plots indicate a decrease of the ageing rate as the cell undergoes more and more charge-discharge cycles. This is best apparent when viewing Fig. 4 a-c,g. There, the Arrhenius plots shown previously are grouped according to the C-rate instead of SoH.

The slope of the Arrhenius lines remains relatively similar at different SoHs and C-rates at low temperatures for commercial cells. However, the slope of the high temperature lines gradually decreases almost to zero with decreasing SoH – best visible in Fig. 4a and b.

In other words, as the cells age, the ageing rates in the temperature range 25 °C–55 °C become very similar. Although the thickness of lithium deposited on the anode has been shown to increase with cycle number nearly linearly for other cell types in a certain range of cycles [20], the SEI growth is a self-passivating phenomenon [8,55]. This passivation is likely the reason for the decreasing temperature dependence of the high temperature term.

As described above, linear fits of specific SoH regions of the capacity fade curves have been used for the determination of the ageing rate (Fig. 2). However, beside considering the slope, one can further consider the y-intercept of the linear fits, which is defined as a virtual SoH at the start of cycling if the ageing behaviour would have been linear overall (SoH$_0$, see Fig. 2). This measure can be used to quantitatively judge the extent to which the ageing behaviour shows accelerated (SoH$_0$ > 100%), decelerated (SoH$_0$ < 100%), or linear (SoH$_0$ = 100%) trends. Consequently, one can evaluate and quantify the overall ageing behaviour by comparing the SoH$_0$ for different battery states and cycling conditions. Changes in the ageing behaviour, e.g. decelerated or accelerated ageing
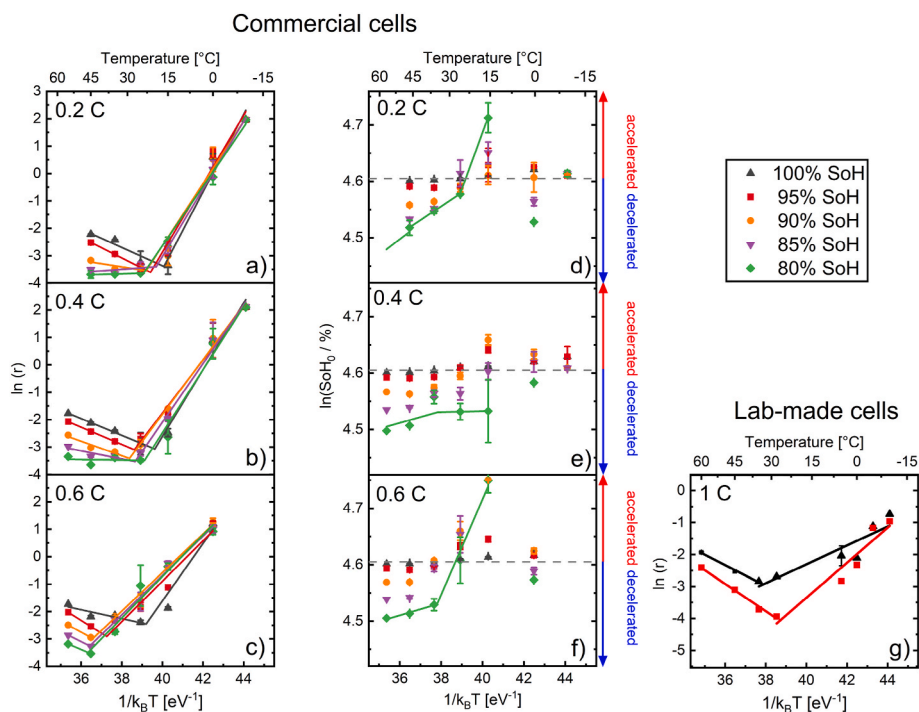
Fig. 4. Arrhenius plots of the ageing rate as a function of SoH with linear fits for commercial cells charged at (a) 0.2C, (b) 0.4C and (c) 0.6C rate; Arrhenius-like plots characterizing the degree to which the capacity fade curves are accelerated or decelerated at (d) 0.2C, (e) 0.4C and (f) 0.6C rate. The dotted line denotes $SoH_0 =$ 100% and the split linear fit for 80% SoH is plotted; (g) Arrhenius plots of the ageing rate as a function of SoH for lab-made cells charged at 1C rate.

behaviour, can be identified by changes of the SoH_0. An Arrhenius-like plot of $\ln(SoH_0)$ versus inverse temperature at different SoHs is shown in Fig. 4d–f. Due to the larger amount of available data we focus on the commercial 21,700 cells.

As shown in Fig. 4d–f, capacity fade curves at high temperatures are decelerated for all SoH and C-rates. This could originate from LLI as the main ageing mechanism [7,20]. Lowering the temperature from 55 °C to 15 °C, the capacity fade curves gradually shift from a decelerated to an accelerated shape, coinciding with the switch in the main ageing mechanism from SEI growth to lithium deposition. The change of the shape of the curves from decelerated to accelerated can be explained by the nature of the underlying ageing mechanism. While SEI growth slows down with ageing and generally can often be described by a square root of time function and therefore correlated with a decreasing rate of ageing [8,19–21], Li deposition is a self-amplifying mechanism.

The accelerated ageing behaviour is mostly observed at temperatures of 15 °C and below, and has been previously correlated to lithium deposition on the anode [6,9]. We indeed see that at temperatures where lithium deposition is the dominating mechanism of ageing (deduced from Arrhenius plots), the fitted SoH_0 values predominantly indicate an

accelerated shape of the capacity fade curves.

The deposition of lithium at lower temperatures is confirmed by the shape of the charge-discharge curves (Fig. 5). In the discharge curves of commercial cells at −10 °C and 0 °C, a voltage plateau is found (Fig. 5a). As previously shown by Smart et al., this feature in the discharge voltage curve is related to lithium stripping and the mixed potential of lithiated graphite in contact with lithium metal [57]. The plateau corresponding to lithium stripping was not observable in the voltage curves of the lab-made cells (Fig. 5b). This could be related to the lower thickness and larger rest times after the charging of the lab-made cells, leading to part of the deposited lithium being re-intercalated before the start of the discharge [46]. Note, however, that some of the material deposited on the electrode may lose electrical connection with the electrode and forms 'dead lithium' regardless of whether sufficient time was allowed for its re-intercalation, as shown by Gao et al. [46]. This is also consistent with accelerated rate calorimetry (ARC) experiments on 18,650 cells with lithium deposition which showed a higher degree of destruction in comparison with cells without Li deposition regardless of the rest time allowing re-intercalation [58]. Hence, dependent on whether some of the lithium is reinserted in the anode or not, lithium
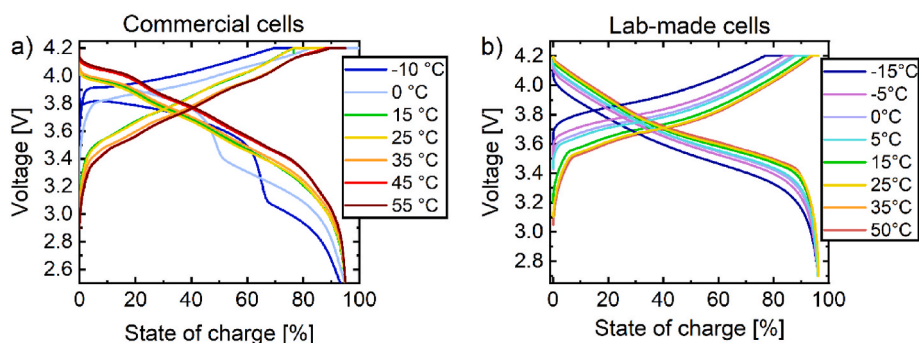

Fig. 5. Charge-discharge curves of (a) commercial cells charged at 0.4C rate at 95% SoH and (b) lab-made cells charged at 0.5C rate at 95% SoH. Discharge profiles with the shape characteristic to stripping of the plated lithium can be clearly observed for commercial cells at −10 °C and 0 °C.

deposition contributes to the ageing of the cell via loss of lithium inventory.

For the 0 °C to −10 °C temperature range, the determination of SoH_0 is extremely challenging due to a relatively fast ageing – we observed most of the commercial cells reach 80% SoH within less than 10 full charge-discharge cycles. Hence, the data analysis for low temperatures is only indicative of the general trend. Moreover, for some capacity fade curves below 85% SoH a shift in the slope is observed (i.e. transition from accelerated to decelerated or vice versa), hence the simple linear fit and intercept cannot be used any more.

Evident from Fig. 4a–c,g, as the cells age, the crossover temperature between the two dominating ageing mechanisms changes. We observe different trends for the commercial and lab-made cells, indicating that the ageing is governed by a complex set of parameters. While the crossover temperature of the lab-made cells shifts downward to lower temperatures, the crossover temperature of the commercial cells largely shifts upwards and is analysed in larger detail in Fig. 6.

For the commercial 21,700 cells, a shift of the crossover temperature towards higher temperatures is observed for all C-rates until 90% SoH. A monotonically increasing trend for the crossover temperature until 80% SoH is only observed for 0.6C. For 0.4C and in parts 0.2C, the trend is reversed below 90% SoH. This is probably an interplay between loss of anode active material (LAAM) and LLI both competing to shift the optimum temperature upwards or lower, respectively. Both processes are discussed in more detail in the next paragraphs.

For the lab-made cells, the minimum in the Arrhenius plot for 1C is shifted from 34 °C for 100% SoH to 27 °C for 95% SoH (Fig. 4g). This decrease of the crossover temperature is in contrast with the observations for the commercial cells. As explained by Petzl et al. [20], LLI leads to less Li deposition at lower SoH since the high SoC region of the negative electrode is not accessible anymore. Therefore, the optimum temperature shifts to lower values. In the lab-made pouch cells, the anode active material consisted of graphite without a Si compound, therefore, LAAM is less likely and the LLI shifts the crossover temperature to lower values.

In contrast, the anode active material of the commercial cells consisted of graphite with ~3% Si, therefore LAAM could have happened, e. g. by film formation on the Si compound [18,59] and the crossover temperature is shifted to higher values. Increasing practical C-rates are likely to blame – although the charge and discharge currents are constant throughout the experiment, if the reduction of capacity is caused
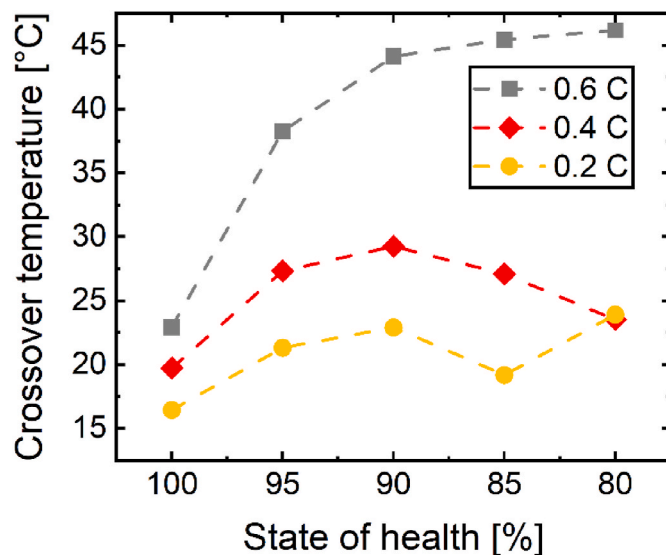
by LAAM, the effective C-rate increases with ageing and the observed effect is similar as discussed above (Fig. 3), where increased C-rates lead to lithium deposition taking place at higher temperatures.

3.4. Practical implications and prediction of cycle life

We have so far shown that the ageing rate of Li-ion cells depends on many factors, including the charging C-rate, SoH, ambient temperature, and electrode coating thickness. As demonstrated in Fig. 7 for the commercial 21,700 cells, these parameters have a significant practical implication regarding the cycle life of the battery cells and can in some cases influence the cycle life by as much as an order of magnitude.

There are even large differences when only one parameter is changed. While the cells can be cycled with 0.2C for 662 cycles until 80% SoH is reached at 25 °C, only approximately half of the cycles can be achieved at 15 °C at the same C-rate (Fig. 7d). Similarly, increasing the charging C-rate to 0.6C at 25 °C leads to an even worse cycle life of 115 cycles. However, compared to the 115 cycles at 25 °C and 0.6C, an ambient temperature of 45 °C can more than triple the cycle life of the cell (387 cycles).

Another practical implication is that the optimum charging temperature varies with SoH. For example, until 95% SoH is reached at 0.4C (Fig. 7a), the largest number of cycles can be accomplished at 25 °C, while more full charge-discharge cycles at the same C-rate were possible at 35 °C until 90% SoH (Fig. 7b). Hence, if heating or cooling of a battery system is used, the battery management system (BMS) also needs to consider the SoH of the cells to choose the optimum temperature and/or charging rate. Meanwhile, the data from the lab-made cells, which have thinner electrodes and more stable active materials, suggest that the optimum operating conditions and evolution of the optimum temperature can vary between cell types in general, and in particular between high-power and high-energy type cells. The shift of optimum temperature with reduced SoH can strongly depend on the cell architecture, including the electrode composition, thickness, porosity, tortuosity, and degree of pre-lithiation.

Besides finding the optimum operating conditions, Arrhenius plots (e.g. Fig. 4a–c) enable the estimation of the ageing rate for every temperature within the considered temperature range. Therefore, it is possible to calculate the EoL of the battery, which is defined by falling below 80% SoH in this case. For a known linearized ageing rate r, the SoH after n cycles can be calculated by

$$SoH(n) = r \cdot n + SoH_0. \tag{2}$$

By setting $SoH(n)$ to EoL, one can calculate the cycles until EoL by

$$n(EoL) = \frac{EoL - SoH_0}{r}. \tag{3}$$

The estimation of the EoL can be done either by a simpler overall linearized or a more complex model, which only linearizes the ageing behaviour in the region of the EoL. For the overall linearized assumption, SoH_0 is set to 100% in equations (2) and (3).

As can be seen in Fig. 8 (dashed line), if one takes the ageing rate at 90% SoH, the overall linearized model fits to the measured number of cycles until the EoL is reached quite well. This can be explained by the fact that the ageing rate at ~90% SoH is very similar to the averaged ageing rate in the range of 100%–80% SoH (for illustration consider the similar slope of the dashed orange fit line at 90% SoH of the decelerated ageing curve and the black dotted linear ageing curve in Fig. 2). Hence, for such a decelerated curve shape, the EoL at 80% SoH can most likely be estimated for every temperature by cycling a comparably small number of battery cells at selected temperatures until 90% SoH.

A more general approach for temperature dependent EoL estimation, which does not depend on the overall ageing behaviour, is shown in Fig. 8 as well (solid line – EoL linear). In this case, the ageing curve is only linearized around the EoL. Hence, the SoH_0 in equation (3) differs from 100% (see discussion of accelerated and decelerated capacity fade

Fig. 6. Crossover temperature between two governing ageing mechanisms of commercial 21,700 cells, determined by the intercept of the two linear fits for low and high temperature ageing behaviour in the Arrhenius plots in Fig. 3a–e.
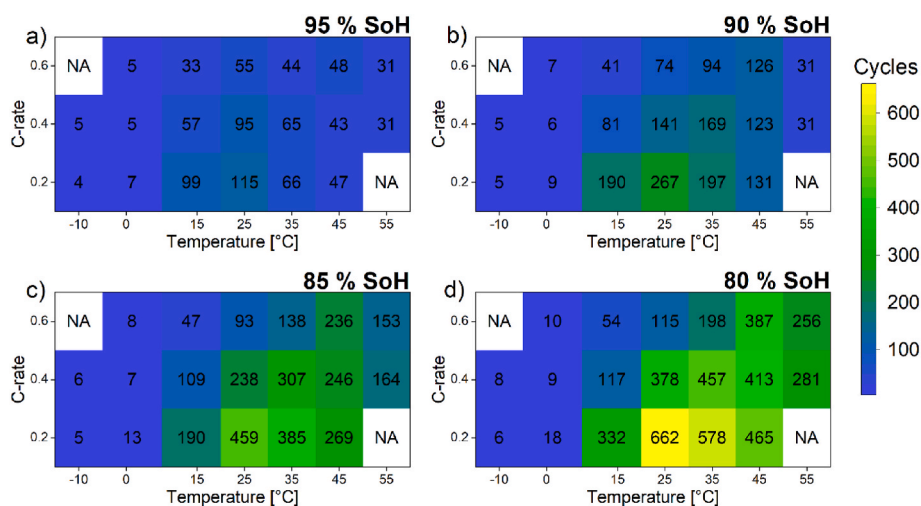
Fig. 7. Experimental results of cycle-life for full charge-discharge cycles of the commercial 21,700 cells until the specified SoH in a heat map as function of C-rate and temperature: (a) 95% SoH, (b) 90% SoH, (c) 85% SoH, (d) 80% SoH.
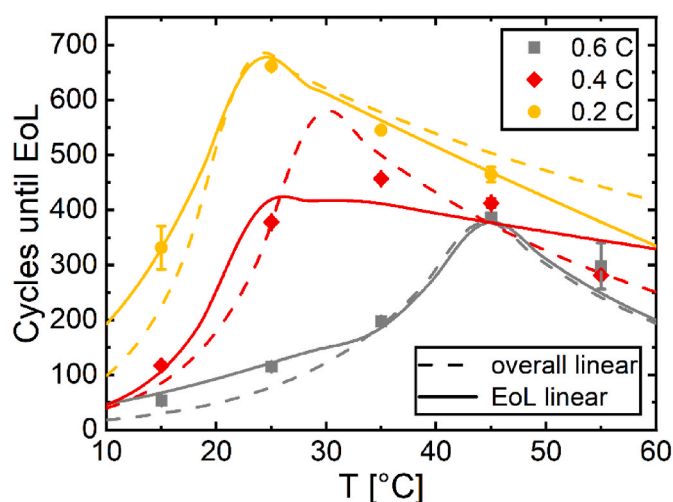

Fig. 8. Estimated (lines) and measured (symbols) cycles until EoL at SoH of 80% is reached. Estimation is done with an overall linear model and ageing rates calculated at 90% SoH (dashed line) and a linearized model based on corresponding linear fits at EoL (solid line).

above). However, SoH_0 can be extracted from the Arrhenius-like plots in Fig. 4d–f for 80% SoH. Although the effort for this model is higher, it is more accurate and more generally valid. Nevertheless, both models offer a simple way to predict the expected cycle life of battery cells with only a small number of cells out of the complete dataset.

4. Conclusions

In this study, extended cycling ageing tests at different ambient temperatures were performed with commercial state-of-the-art 21,700 cells (Si/graphite vs. NCA/LNO) and with lab-made pouch cells (graphite vs. NMC). Arrhenius plots were constructed from the ageing rates considering variations of C-rates for different SoHs and under consideration of the capacity fade curve shapes. The Arrhenius plots showed minima which shift with these parameters. The minima correspond to a crossover temperature between the main ageing mechanisms of SEI growth and Li deposition.

The key trends observed in our study are:

1) Charging C-rate: Larger charging rates generally lead to a higher crossover temperature.
2) State of health: Aged and fresh cells do not display the same ageing behaviour if the capacity fade curves are non-linear. The correlation is therefore complex and depends most likely on the cell chemistry and the electrodes. We were able to observe a crossover temperature increase for one type of cell and a decrease for another. This is most likely affected by LLI in case of the cells with graphite anodes and by LAAM in case of the cells with Si/graphite anode.
3) Anode coating thickness in combination with particle size in the anode: The thinner the electrode and the smaller the anode active material particles, the lower the crossover temperature at the same rate of charging, i.e. thinner negative electrodes with smaller particles in high-power cells are most likely less prone to lithium deposition compared to high-energy cells with thicker negative electrodes with similar porosity and larger particles.

Additionally, two ways to model the temperature dependent EoL are shown. Especially when considering the SoH_0 from the fits at EoL, the EoL could be estimated precisely and could provide valuable data for further use in e.g. BMS with reduced effort in ageing tests.

The presented results are most likely general trends since they were observed for two different cell types. However, the exact parametrization is most likely different for each cell type. To evaluate and optimize the ageing behaviour of cells as a function of their architecture (i.e. electrode thickness, areal loading, porosity, N/P ratio, active material, microstructure, etc.) and operational conditions (e.g. fast-charging conditions), further experimental and theoretical calculations are needed. To encourage theoretical studies, we have provided the data on the architecture of both types of cells used in our work. Further experiments in this direction are underway in our labs.

CRediT authorship contribution statement

Gints Kucinskis: Conceptualization, Investigation, Visualization, Data curation, Funding acquisition, Writing – original draft. **Maral Bozorgchenani:** Conceptualization, Investigation, Visualization, Data curation, Writing – original draft. **Max Feinauer:** Conceptualization, Investigation, Methodology, Visualization, Data curation, Writing – original draft, Writing – review & editing. **Michael Kasper:** Conceptualization, Investigation, Methodology, Data curation, Writing – review & editing. **Margret Wohlfahrt-Mehrens:** Conceptualization, Resources, Supervision, Funding acquisition, Writing – review & editing. **Thomas Waldmann:** Conceptualization, Resources, Supervision, Project

administration, Funding acquisition, Writing – original draft, Writing – review & editing.

Declaration of competing interest

The authors declare that they have no known competing financial interests or personal relationships that could have appeared to influence the work reported in this paper.

Data availability

Data will be made available on request.

Acknowledgements

Appendix A. Supplementary data

Supplementary data to this article can be found online at https://doi.org/10.1016/j.jpowsour.2022.232129.

References

[1] K. Edström, R. Dominko, M. Fichtner, T. Otuszewski, S. Perraud, C. Punckt, J.-M. Tarascon, T. Vegge, M. Winter, Inventing the Sustainable Batteries of the Future: Research Needs and Future Actions, BATTERY 2030+ Roadmap, 2019. https://battery2030.eu/wp-content/uploads/2021/08/c_860904-l_1-k_roadmap-27-march.pdf.

[2] M.M. Kabir, D.E. Demirocak, Degradation mechanisms in Li-ion batteries: a state-of-the-art review, Int. J. Energy Res. 41 (2017) 1963–1986, https://doi.org/10.1002/er.3762.

[3] T. Joshi, K. Eom, G. Yushin, T.F. Fuller, Effects of dissolved transition metals on the electrochemical performance and SEI growth in lithium-ion batteries, J. Electrochem. Soc. 161 (2014) A1915–A1921, https://doi.org/10.1149/2.0861412jes.

[4] M. Dubarry, B.Y. Liaw, M.-S. Chen, S.-S. Chyan, K.-C. Han, W.-T. Sie, S.-H. Wu, Identifying battery aging mechanisms in large format Li ion cells, J. Power Sources 196 (2011) 3420–3425, https://doi.org/10.1016/j.jpowsour.2010.07.029.

[5] M. Dubarry, V. Svoboda, R. Hwu, B. Yann Liaw, Incremental capacity analysis and close-to-equilibrium OCV measurements to quantify capacity fade in commercial rechargeable lithium batteries, Electrochem. Solid State Lett. 9 (2006) A454, https://doi.org/10.1149/1.2221767.

[6] T. Waldmann, M. Wilka, M. Kasper, M. Fleischhammer, M. Wohlfahrt-Mehrens, Temperature dependent ageing mechanisms in Lithium-ion batteries – a Post-Mortem study, J. Power Sources 262 (2014) 129–135, https://doi.org/10.1016/j.jpowsour.2014.03.112.

[7] T. Waldmann, B.-I. Hogg, M. Wohlfahrt-Mehrens, Li plating as unwanted side reaction in commercial Li-ion cells – a review, J. Power Sources 384 (2018) 107–124, https://doi.org/10.1016/j.jpowsour.2018.02.063.

[8] M. Broussely, S. Herreyre, P. Biensan, P. Kasztejna, K. Nechev, R. Staniewicz, Aging mechanism in Li ion cells and calendar life predictions, J. Power Sources 97–98 (2001) 13–21, https://doi.org/10.1016/S0378-7753(01)00722-4.

[9] J.C. Burns, D.A. Stevens, J.R. Dahn, In-situ detection of lithium plating using high precision coulometry, J. Electrochem. Soc. 162 (2015) A959–A964, https://doi.org/10.1149/2.0621506jes.

[10] P. Taheri, S. Hsieh, M. Bahrami, Investigating electrical contact resistance losses in lithium-ion battery assemblies for hybrid and electric vehicles, J. Power Sources 196 (2011) 6525–6533, https://doi.org/10.1016/j.jpowsour.2011.03.056.

[11] V. Agubra, J. Fergus, Lithium ion battery anode aging mechanisms, Materials 6 (2013) 1310–1325, https://doi.org/10.3390/ma6041310.

[12] C. Lin, A. Tang, H. Mu, W. Wang, C. Wang, Aging mechanisms of electrode materials in lithium-ion batteries for electric vehicles, J. Chem. 2015 (2015) 1–11, https://doi.org/10.1155/2015/104673.

[13] S. Tippmann, D. Walper, L. Balboa, B. Spier, W.G. Bessler, Low-temperature charging of lithium-ion cells part I: electrochemical modeling and experimental investigation of degradation behavior, J. Power Sources 252 (2014) 305–316, https://doi.org/10.1016/j.jpowsour.2013.12.022.

[14] A. Nuhic, T. Terzimehic, T. Soczka-Guth, M. Buchholz, K. Dietmayer, Health diagnosis and remaining useful life prognostics of lithium-ion batteries using data-driven methods, J. Power Sources 239 (2013) 680–688, https://doi.org/10.1016/j.jpowsour.2012.11.146.

[15] K.A. Severson, P.M. Attia, N. Jin, N. Perkins, B. Jiang, Z. Yang, M.H. Chen, M. Aykol, P.K. Herring, D. Fraggedakis, M.Z. Bazant, S.J. Harris, W.C. Chueh, R. D. Braatz, Data-driven prediction of battery cycle life before capacity degradation, Nat. Energy 4 (2019) 383–391, https://doi.org/10.1038/s41560-019-0356-8.

[16] X.-G. Yang, Y. Leng, G. Zhang, S. Ge, C.-Y. Wang, Modeling of lithium plating induced aging of lithium-ion batteries: transition from linear to nonlinear aging, J. Power Sources 360 (2017) 28–40, https://doi.org/10.1016/j.jpowsour.2017.05.110.

[17] S.F. Schuster, T. Bach, E. Fleder, J. Müller, M. Brand, G. Sextl, A. Jossen, Nonlinear aging characteristics of lithium-ion cells under different operational conditions, J. Energy Storage 1 (2015) 44–53, https://doi.org/10.1016/j.est.2015.05.003.

[18] K. Richter, T. Waldmann, N. Paul, N. Jobst, R. Scurtu, M. Hofmann, R. Gilles, M. Wohlfahrt-Mehrens, Low-temperature charging and aging mechanisms of Si/C composite anodes in Li-ion batteries: an operando neutron scattering study, ChemSusChem 13 (2020) 529–538, https://doi.org/10.1002/cssc.201903139.

[19] T.C. Bach, S.F. Schuster, E. Fleder, J. Müller, M.J. Brand, H. Lorrmann, A. Jossen, G. Sextl, Nonlinear aging of cylindrical lithium-ion cells linked to heterogeneous compression, J. Energy Storage 5 (2016) 212–223, https://doi.org/10.1016/j.est.2016.01.003.

[20] M. Petzl, M. Kasper, M.A. Danzer, Lithium plating in a commercial lithium-ion battery – a low-temperature aging study, J. Power Sources 275 (2015) 799–807, https://doi.org/10.1016/j.jpowsour.2014.11.065.

[21] D.A. Stevens, R.Y. Ying, R. Fathi, J.N. Reimers, J.E. Harlow, J.R. Dahn, Using high precision coulometry measurements to compare the degradation mechanisms of NMC/LMO and NMC-only automotive scale pouch cells, J. Electrochem. Soc. 161 (2014) A1364–A1370, https://doi.org/10.1149/2.0971409jes.

[22] P.W. Atkins, Physical Chemistry, fourth ed., Oxford University Press, 1990.

[23] F. Helfferich, Kinetics of Multistep Reactions, second ed., Elsevier, 2004.

[24] S. Käbitz, J.B. Gerschler, M. Ecker, Y. Yurdagel, B. Emmermacher, D. André, T. Mitsch, D.U. Sauer, Cycle and calendar life study of a graphite|LiNi1/3Mn1/3Co1/3O2 Li-ion high energy system. Part A: full cell characterization, J. Power Sources 239 (2013) 572–583, https://doi.org/10.1016/j.jpowsour.2013.03.045.

[25] B.Y. Liaw, E.P. Roth, R.G. Jungst, G. Nagasubramanian, H.L. Case, D.H. Doughty, Correlation of Arrhenius behaviors in power and capacity fades with cell impedance and heat generation in cylindrical lithium-ion cells, J. Power Sources 119–121 (2003) 874–886, https://doi.org/10.1016/S0378-7753(03)00196-4.

[26] I. Bloom, B. Cole, J. Sohn, S. Jones, E. Polzin, V. Battaglia, G. Henriksen, C. Motloch, R. Richardson, T. Unkelhaeuser, D. Ingersoll, H. Case, An accelerated calendar and cycle life study of Li-ion cells, J. Power Sources 101 (2001) 238–247, https://doi.org/10.1016/S0378-7753(01)00783-2.

[27] M.C. Smart, J.F. Whitacre, B.V. Ratnakumar, K. Amine, Electrochemical performance and kinetics of Li1+x(Co1/3Ni1/3Mn1/3)1−xO2 cathodes and graphite anodes in low-temperature electrolytes, J. Power Sources 168 (2007) 501–508, https://doi.org/10.1016/j.jpowsour.2006.10.106.

[28] T. Waldmann, M. Kasper, M. Wohlfahrt-Mehrens, Optimization of charging strategy by prevention of lithium deposition on anodes in high-energy lithium-ion batteries – electrochemical experiments, Electrochim. Acta 178 (2015) 525–532, https://doi.org/10.1016/j.electacta.2015.08.056.

[29] Y. Preger, H.M. Barkholtz, A. Fresquez, D.L. Campbell, B.W. Juba, J. Romàn-Kustas, S.R. Ferreira, B. Chalamala, Degradation of commercial lithium-ion cells as a function of chemistry and cycling conditions, J. Electrochem. Soc. 167 (2020), 120532, https://doi.org/10.1149/1945-7111/abae37.

[30] T. Waldmann, B.-I. Hogg, M. Kasper, S. Grolleau, C.G. Couceiro, K. Trad, B. P. Matadi, M. Wohlfahrt-Mehrens, Interplay of operational parameters on lithium deposition in lithium-ion cells: systematic measurements with reconstructed 3-electrode pouch full cells, J. Electrochem. Soc. 163 (2016) A1232–A1238, https://doi.org/10.1149/2.0591607jes.

[31] X.-G. Yang, C.-Y. Wang, Understanding the trilemma of fast charging, energy density and cycle life of lithium-ion batteries, J. Power Sources 402 (2018) 489–498, https://doi.org/10.1016/j.jpowsour.2018.09.069.

[32] J. Liang, Y. Gan, M. Yao, Y. Li, Numerical analysis of capacity fading for a LiFePO4 battery under different current rates and ambient temperatures, Int. J. Heat Mass Tran. 165 (2021), 120615, https://doi.org/10.1016/j.ijheatmasstransfer.2020.120615.

[33] J. Dahn, Structure and electrochemistry of Li1±yNiO2 and a new Li2NiO2 phase with the Ni (OH)2 structure, Solid State Ionics 44 (1990) 87–97, https://doi.org/10.1016/0167-2738(90)90049-W.

[34] H. Lee, S.-K. Chang, E.-Y. Goh, J.-Y. Jeong, J.H. Lee, H.-J. Kim, J.-J. Cho, S.-T. Hong, Li 2 NiO 2 as a novel cathode additive for overdischarge protection of Li-ion batteries, Chem. Mater. 20 (2008) 5–7, https://doi.org/10.1021/cm702290p.

[35] F. Wang, B. Wang, J. Li, B. Wang, Y. Zhou, D. Wang, H. Liu, S. Dou, Prelithiation: a crucial strategy for boosting the practical application of next-generation lithium

ion battery, ACS Nano 15 (2021) 2197–2218, https://doi.org/10.1021/acsnano.0c10664.

[36] H. Park, T. Yoon, Y.-U. Kim, J.H. Ryu, S.M. Oh, Li2NiO2 as a sacrificing positive additive for lithium-ion batteries, Electrochim. Acta 108 (2013) 591–595, https://doi.org/10.1016/j.electacta.2013.06.117.

[37] L. Mauler, F. Duffner, J. Leker, Economies of scale in battery cell manufacturing: the impact of material and process innovations, Appl. Energy 286 (2021), 116499, https://doi.org/10.1016/j.apenergy.2021.116499.

[38] M. Greenwood, M. Wentker, J. Leker, A bottom-up performance and cost assessment of lithium-ion battery pouch cells utilizing nickel-rich cathode active materials and silicon-graphite composite anodes, J. Power Sources Adv. 9 (2021), 100055, https://doi.org/10.1016/j.powera.2021.100055.

[39] J. Xu, Y. Dou, Z. Wei, J. Ma, Y. Deng, Y. Li, H. Liu, S. Dou, Recent progress in graphite intercalation compounds for rechargeable metal (Li, Na, K, Al)-Ion batteries, Adv. Sci. 4 (2017), 1700146, https://doi.org/10.1002/advs.201700146.

[40] E. Moyassari, T. Roth, S. Kücher, C.-C. Chang, S.-C. Hou, F.B. Spingler, A. Jossen, The role of silicon in silicon-graphite composite electrodes regarding specific capacity, cycle stability, and expansion, J. Electrochem. Soc. 169 (2022), 010504, https://doi.org/10.1149/1945-7111/ac4545.

[41] M. Shi, Z. Tai, N. Li, K. Zou, Y. Chen, J. Sun, Y. Liu, Spherical graphite produced from waste semi-coke with enhanced properties as an anode material for Li-ion batteries, Sustain. Energy Fuels 3 (2019) 3116–3127, https://doi.org/10.1039/C9SE00606K.

[42] C. Erk, T. Brezesinski, H. Sommer, R. Schneider, J. Janek, Toward silicon anodes for next-generation lithium ion batteries: a comparative performance study of various polymer binders and silicon nanopowders, ACS Appl. Mater. Interfaces 5 (2013) 7299–7307, https://doi.org/10.1021/am401642c.

[43] J.B. Quinn, T. Waldmann, K. Richter, M. Kasper, M. Wohlfahrt-Mehrens, Energy density of cylindrical Li-ion cells: a comparison of commercial 18650 to the 21700 cells, J. Electrochem. Soc. 165 (2018) A3284–A3291, https://doi.org/10.1149/2.0281814jes.

[44] M. Bozorgchenani, G. Kucinskis, M. Wohlfahrt-Mehrens, T. Waldmann, Experimental confirmation of C-rate dependent minima shifts in Arrhenius plots of Li-ion battery aging, J. Electrochem. Soc. 169 (2022), 030509, https://doi.org/10.1149/1945-7111/ac580d.

[45] K. Eberman, P. Gomadam, G. Jain, E. Scott, Material and design options for avoiding lithium plating during charging, ECS Trans. 25 (2010) 47–58, https://doi.org/10.1149/1.3414003.

[46] T. Gao, Y. Han, D. Fraggedakis, S. Das, T. Zhou, C.-N. Yeh, S. Xu, W.C. Chueh, J. Li, M.Z. Bazant, Interplay of lithium intercalation and plating on a single graphite particle, Joule 5 (2021) 393–414, https://doi.org/10.1016/j.joule.2020.12.020.

[47] K.G. Gallagher, S.E. Trask, C. Bauer, T. Woehrle, S.F. Lux, M. Tschech, P. Lamp, B. J. Polzin, S. Ha, B. Long, Q. Wu, W. Lu, D.W. Dees, A.N. Jansen, Optimizing areal capacities through understanding the limitations of lithium-ion electrodes, J. Electrochem. Soc. 163 (2016) A138–A149, https://doi.org/10.1149/2.0321602jes.

[48] T.L. Kulova, A.M. Skundin, E.A. Nizhnikovskii, A.V. Fesenko, Temperature effect on the lithium diffusion rate in graphite, Russ. J. Electrochem. 42 (2006) 259–262, https://doi.org/10.1134/S1023193506030086.

[49] C. Hogrefe, T. Waldmann, M.B. Molinero, L. Wildner, P. Axmann, M. Wohlfahrt-Mehrens, Cross-sectional in situ optical microscopy with simultaneous electrochemical measurements for lithium-ion full cells, J. Electrochem. Soc. 169 (2022), 050519, https://doi.org/10.1149/1945-7111/ac6c57.

[50] N. Ghanbari, T. Waldmann, M. Kasper, P. Axmann, M. Wohlfahrt-Mehrens, Inhomogeneous degradation of graphite anodes in Li-ion cells: a postmortem study using glow discharge optical emission spectroscopy (GD-OES), J. Phys. Chem. C 120 (2016) 22225–22234, https://doi.org/10.1021/acs.jpcc.6b07117.

[51] N. Ghanbari, T. Waldmann, M. Kasper, P. Axmann, M. Wohlfahrt-Mehrens, Detection of Li deposition by glow discharge optical emission spectroscopy in post-mortem analysis, ECS Electrochem. Lett. 4 (2015) A100–A102, https://doi.org/10.1149/2.0041509eel.

[52] A. Iturrondobeitia, F. Aguesse, S. Genies, T. Waldmann, M. Kasper, N. Ghanbari, M. Wohlfahrt-Mehrens, E. Bekaert, Post-mortem analysis of calendar-aged 16 Ah NMC/graphite pouch cells for EV application, J. Phys. Chem. C 121 (2017) 21865–21876, https://doi.org/10.1021/acs.jpcc.7b05416.

[53] T. Waldmann, J.B. Quinn, K. Richter, M. Kasper, A. Tost, A. Klein, M. Wohlfahrt-Mehrens, Electrochemical, post-mortem, and ARC analysis of Li-ion cell safety in second-life applications, J. Electrochem. Soc. 164 (2017) A3154–A3162, https://doi.org/10.1149/2.0961713jes.

[54] P.M. Attia, W.C. Chueh, S.J. Harris, Revisiting the t 0.5 dependence of SEI growth, J. Electrochem. Soc. 167 (2020), 090535, https://doi.org/10.1149/1945-7111/ab8ce4.

[55] L. Kolzenberg, A. Latz, B. Horstmann, Solid–electrolyte interphase during battery cycling: theory of growth regimes, ChemSusChem 13 (2020) 3901–3910, https://doi.org/10.1002/cssc.202000867.

[56] P.M. Attia, S. Das, S.J. Harris, M.Z. Bazant, W.C. Chueh, Electrochemical kinetics of SEI growth on carbon black: Part I. Experiments, J. Electrochem. Soc. 166 (2019) E97–E106, https://doi.org/10.1149/2.0231904jes.

[57] M.C. Smart, B.V. Ratnakumar, K.B. Chin, L.D. Whitcanack, S. Surampudi, Performance characteristics of lithium-ion technology under extreme environmental conditions, in: Int. Energy Convers. Eng. Conf. IECEC, 1st, 2003, https://doi.org/10.2514/6.2003-5984.

[58] T. Waldmann, M. Wohlfahrt-Mehrens, Effects of rest time after Li plating on safety behavior—ARC tests with commercial high-energy 18650 Li-ion cells, Electrochim, Acta 230 (2017) 454–460, https://doi.org/10.1016/j.electacta.2017.02.036.

[59] M. Flügel, K. Richter, M. Wohlfahrt-Mehrens, T. Waldmann, Detection of Li deposition on Si/graphite anodes from commercial Li-ion cells: a post-mortem GD-OES depth profiling study, J. Electrochem. Soc. 169 (2022), 050533, https://doi.org/10.1149/1945-7111/ac70af.